Japan) were implanted into the region of the thalamus in the left hemispheres of the brains of 20 rats (8 weeks old, 292.8 ± 14.8 g). The implantation procedures were performed under general anesthesia using an intramuscular injection of ketamine (33 mg/kg; Sankyo Co., Ltd., Tokyo, Japan) and xylazine (7 mg/kg; Bayer AG, Leverkusen, Germany). A burr hole was made 3 mm lateral and 2 mm posterior to the bregma using a dental drill. A needle with an outer diameter of 0.3 mm was inserted 4 mm below the outer table of the skull through the burr hole. A 10-μl solution containing 10^7 cells/ml was infused over 5 min at a constant rate using a microsyringe (Hamilton Co., Reno, Nev., USA) and infusion pump (Eicom Corp., Kyoto, Japan).

MR imaging. Two weeks after implantation, all 20 rats underwent screening by T1W imaging after Gd-DTPA administration. Developed glioma was confirmed in only five out of 20 rats. Those five rats were used for experiments for the comparison of pulse sequences. Three weeks after implantation, when the glioma was fully developed, T1W brain images of the selected five rats (11 weeks old, 301.3 ± 29.0 g) were acquired before and after Gd-DTPA administration using three pulse sequences determined by the phantom study (Table 2) in the coronal plane. Rats were given general anesthesia with an intramuscular injection of a ketamine (33 mg/kg) and xylazine (7 mg/kg) mixture, and allowed to breathe spontaneously during preparation and imaging. First, precontrast T1W images were acquired. Then, a dose of 0.1 mmol/kg of Gd-DTPA was administered by hand injection followed by a 3.0-ml saline flush through a 22G indwelling needle placed in a tail or femoral vein. Postcontrast T1W imaging started 1 min after Gd-DTPA administration with identical settings to the precontrast imaging. Each rat was examined using all three pulse sequences (Table 2). In order to eliminate the effect of previously administered Gd-DTPA, three scans using different pulse sequences

were performed on three separate days, at 22- to 26-hour intervals, in a randomized order.

ROI analysis. Based on the results of histopathology (see below), ROIs were placed on a portion of each glioma. Areas of necrosis or hemorrhage were excluded from the ROI. Mean signal intensities in the pre- and postcontrast T1W images were calculated from each ROI. For each sequence, signal enhancement of each glioma (E_T) was calculated as $E_T = S_{post}/S_{pre}$, where S_{post} is signal intensity in the glioma after contrast and S_{pre} is that before contrast.

Histopathology
One day after MR imaging, rat brains were removed and fixed in formalin. All brains were completely coronally sectioned. Sections were stained with hematoxylin and eosin (HE) in order to delineate areas of glioma, hemorrhage, and necrosis.

Statistical analysis
All parameters assessed were given as means $\pm$ standard deviations. Pair-wise comparison among pulse sequences was performed using the Tukey-Kramer test. A P value of <0.05 was considered statistically significant.

Results

T1 in normal rat brains
Fig. 2 shows images from one of the three normal rats used to quantitate T1 values in the brain. Table 3 summarizes the T1 values of typical brain structures. The T1 value in the thalamus was 1405 ± 32 ms.

T1 of Gd-DTPA solutions
Fig. 3 shows selected images from a series of 17 images obtained with different TR values. Table 4 summarizes T1 values in the Gd-DTPA solutions

Table 2. Pulse sequences and imaging parameters used for imaging of rat brains with C6 glioma cell implants

Pulse sequence	TR, ms	TE, ms	FA, °	ETL	BW, kHz	NEX	Acquisition time, min:s
SE	1400	13	—	—	16	1	4:46
FSE	1400	18.6	—	3	32	3	4:32
FSPGR	20	4.7	30	—	32	8	5:40

For all pulse sequences, FOV was 60×45 mm, matrix was 256×192, the number of slices was 11, and the slice thickness was 2.5 mm (0.5-mm gap). SE: spin echo; FSE: fast spin echo; FSPGR: fast spoiled gradient echo; TR: repetition time; TE: echo time; FA: flip angle; ETL: echo train length; BW: bandwidth; NEX: number of excitations.
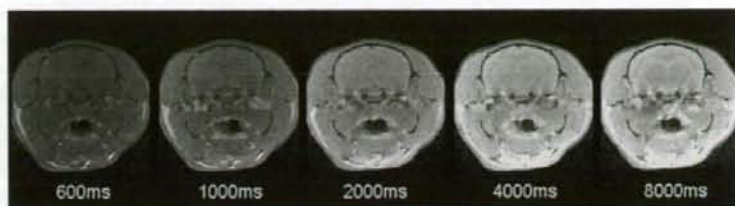
262880

Fig. 2. Images from one of three rats used for the measurement of T1 values in normal rat brain. One of 16 slices acquired is shown. The images are arranged from left to right in ascending order of repetition time. All five images are set with equal window width and equal window level.

Table 3. T1 relaxation time in normal rat brain at 3T

	T1, ms
Thalamus	1405 ± 32
Hippocampus	1779 ± 151
Olfactory bulb	1613 ± 117
Cerebral cortex	1506 ± 13
Corpus callosum	1389 ± 43
Midbrain	1329 ± 50
Cerebellum	1726 ± 356
Pons	1343 ± 80
Cerebrospinal fluid	3460 ± 737
Muscle	1529 ± 99

Mean and standard deviation of values obtained from three rats.

ranging from 0 to 10 mM. In 30 and 50 mM solutions, an accurate T1 value could not be measured because of extensive signal loss due to T2 decay. The 0.1-mM solution showed a T1 value (1302 ± 54 ms) closest to that in the normal thalamus (1405 ± 32 ms).
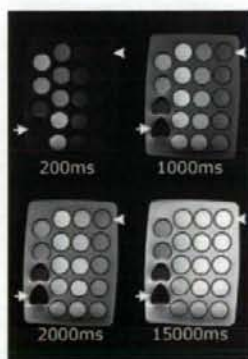

Fig. 3. Images obtained in the measurement of T1 values of 19 saline solutions with different concentrations of gadopentetate dimeglumine (0, 0.01, 0.03, 0.05, 0.07, 0.1, 0.15, 0.2, 0.25, 0.3, 0.5, 0.7, 1, 3, 5, 7, 10, 30, and 50 mM). The four selected images from a series of 17 images obtained with different TR values are shown. Each solution was encapsulated in separate polypropylene vials, which were set in agar. The concentration of gadopentetate dimeglumine decreases from bottom to top and from left to right. Arrows and arrowheads denote the 50-mM and 0-mM solutions, respectively. All four images are set with equal window width and equal window level.

Table 4. T1 of saline with different concentrations of Gd-DTPA at 3T

Gd-DTPA concentration, mM	T1, ms
0	3026 ± 121
0.01	2652 ± 96
0.03	2245 ± 108
0.05	1970 ± 92
0.07	1775 ± 103
0.1	1302 ± 54
0.15	993 ± 57
0.2	820 ± 52
0.25	737 ± 51
0.3	666 ± 63
0.5	389 ± 17
0.7	284 ± 12
1	209 ± 9
3	84 ± 4
5	58 ± 2
7	36 ± 1
10	27 ± 1
30	—
50	—

Mean and standard deviation of values obtained from five measurements.

Choice of pulse sequences

Fig. 4 shows E_P in the Gd-DTPA solutions ranging from 0.1 to 50 mM. In Gd-DTPA solutions ranging from 0.15 to 30 mM, a higher E_P was obtained as follows: FSPGR > SE > FSE > T1FLAIR. Because E_P for T1FLAIR was lowest at all concentrations, T1FLAIR was not used for the imaging of rat brain tumors.

Based on our preliminary experiments, the T1 value in the glioma in the thalamus region after contrast was about 90% of that before contrast. Therefore, we regarded the 0.15-mM solution as a corresponding solution to glioma after contrast, and compared E_P values at 0.15 mM obtained using different sequences (Fig. 5). E_P at 0.15 mM was 1.10 ± 0.02 for FSE, 1.16 ± 0.01 for FSPGR, 1.16 ± 0.01 for SE, and 1.06 ± 0.01 for T1FLAIR. The Tukey-Kramer test showed significant differences ($P < 0.05$) between all pairs except for FSPGR–SE. E_P for FSPGR was significantly higher than that for FSE and T1FLAIR and comparable to that for SE.
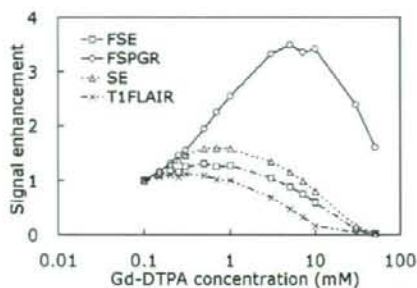
Acta Radiol 2007 (000)

87

262880

Fig. 4. Signal enhancements in saline solutions containing gado-pentetate dimeglumine (Gd-DTPA) obtained by the following pulse sequences: spin echo (SE); fast spin echo (FSE); inversion recovery fast spin echo (T1FLAIR); fast spoiled gradient echo (FSPGR). Signal enhancement was the signal intensity scaled by that of a 0.1-mM Gd-DTPA solution whose T1 value was closest to the average T1 value in the brain parenchyma of normal rats.

Signal enhancement in rat brain C6 glioma

Fig. 6 displays typical pre- and postcontrast T1W images of brains of C6 glioma model rats, together with an example of ROIs placed on the glioma and HE-stained slices. Fig. 7 shows the comparison between E_T values for FSE, SE, and FSPGR. E_T values were 1.12 ± 0.05 for FSE, 1.26 ± 0.11 for FSPGR, and 1.20 ± 0.11 for SE. The Tukey-Kramer test showed the significant superiority of FSPGR over FSE. There was no significant difference between FSPGR and SE.

Discussion

T1W imaging using SE results in a corresponding restriction in the number of slices as a result of the
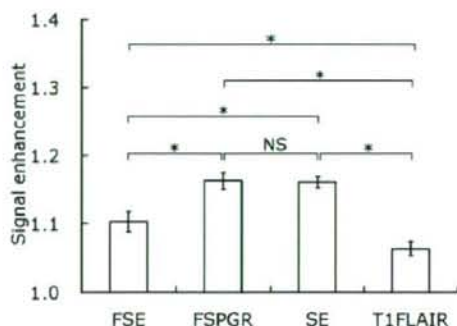

Fig. 5. Signal enhancement of saline solution with 0.15 mM Gd-DTPA obtained using different pulse sequences: spin echo (SE); fast spin echo (FSE); inversion recovery fast spin echo (T1FLAIR); fast spoiled gradient echo (FSPGR). Signal enhancement was defined as the signal intensity of a 0.15-mM solution scaled by that of a 0.1-mM solution. The Tukey-Kramer test was performed for pair-wise comparison among four pulse sequences. The asterisk and NS denote significant difference ($P < 0.05$) and no significant difference ($P > 0.05$), respectively.
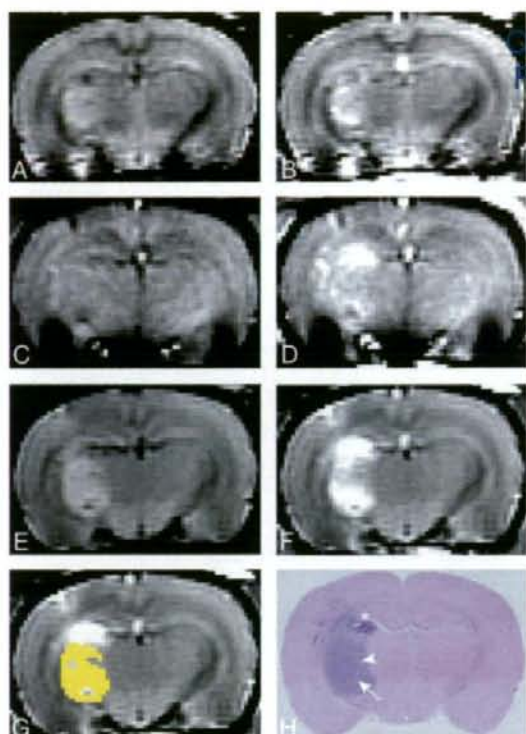

Fig. 6. Examples of pre- (A, C, E) and post-contrast (B, D, F) coronal T1-weighted images obtained using fast spin-echo (FSE) (A, B), fast spoiled gradient-echo (FSPGR) (C, D), and spin-echo (SE) (E, F) sequences. A region of interest (ROI) placed on the glioma (G) and a slice stained using hematoxylin and eosin (HE) (H). T1-weighted images were acquired 3 weeks after the implantation of C6 glioma cells. Areas of necrosis or hemorrhage, which were delineated based on histopathology, were excluded from ROIs. In the HE-stained slice, small-cell glioma (arrowhead), hemorrhage (asterisk), and necrosis (arrow) were found.
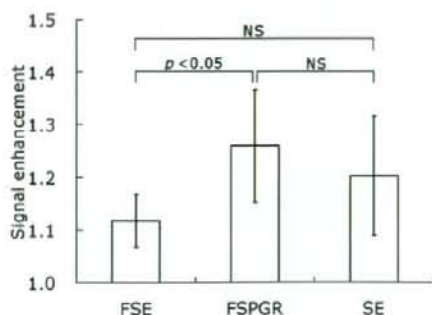

Fig. 7. Signal enhancement in rat brain C6 glioma obtained with different pulse sequences: spin echo (SE); fast spin echo (FSE); fast spoiled gradient echo (FSPGR). Signal enhancement was defined as the signal intensity after Gd-DTPA administration scaled by that before administration. The pair-wise comparison among pulse sequences was performed using the Tukey-Kramer test. NS denotes no significant difference ($P > 0.05$).

specific absorption rate (SAR) at 3T. The use of FSE makes radiofrequency heating more serious. Compared to SE and FSE, FSPGR provides relatively low radiofrequency heating and, if the NEX of FSPGR can be reduced, relatively short acquisition time. This depends on the signal-to-noise ratio, and we thought it possible based on our rat brain images (Fig. 6). Therefore, we examined the characteristics of signal enhancement in FSPGR. FSPGR provided significantly higher signal enhancement than FSE and comparable signal enhancement to SE, both in the 0.15-mM Gd-DTPA solution and in rat brain C6 glioma in the thalamus region. We speculate that FSPGR may be superior to FSE and comparable to SE in its ability to delineate brain tumors, although, in order to verify this speculation, several studies would be required using different cell types and various transplantation sites. Considering the advantage of FSPGR in terms of acquisition time and SAR limit, FSPGR may be more suitable for contrast-enhanced T1W imaging of brain tumors in clinical 3T scanners than SE. Additionally, high-resolution 3D images can be obtained by using FSPGR with a reasonable acquisition time so that small lesions may be better visualized. On the other hand, FSPGR was more sensitive to magnetic suscept-ibility artifacts than SE (Fig. 6). SE could therefore be more suitable than FSPGR for delineation of tumors in regions with susceptibility artifacts, such as the base of the skull.

E_T values obtained in our study (1.26 for FSPGR, 1.20 for SE, and 1.12 for FSE) were lower compared to previously reported values (1, 4, 5, 12). For example, RUNGE et al. reported that the E_T induced by Gd-DTPA was approximately 1.44 using SE in rat brain C6/LacZ glioma models at 3T (5). The difference between E_T in our study and that in previous reports may result from the difference in the type of tumor, in the degree of growth of brain tumors, or in TR. In our study, TR was adjusted to increase T1 contrast in the normal brain region for specification of more exact location of the glioma. Although the use of a shorter TR may increase signal enhancement in the glioma, contrast in the normal region would become unclear, and therefore it could become difficult to specify the location of the glioma exactly. Therefore, we used a longer TR than that in previous reports.

FISCHBACH et al. showed higher contrast in SE in patients, but they optimized the TR (600 ms) of SE by phantom experiments using a saline solution with a low concentration of Gd-DTPA (0.125 μM) (12), whose T1 is extremely long compared to that in the brain. We quantified T1 in rat brains and chose a proper TR (1400 ms) of SE to enhance normal brain contrast. Therefore, our comparison would be fairer and our results may be more closely extrapolated to human tumors.

One limitation of our work is our limited sample size. Although C6 glioma cells were implanted into 20 rats in our in-vivo study, only five rats could be used for the experiment, as C6 gliomas showed considerable individual variation in their growth and were fully developed only in five rats. Therefore, the number of test animals was relatively small, resulting in large standard deviations for E_T. A larger sample size may show a significant difference between FSPGR and SE.

In conclusion, FSPGR is superior to FSE and comparable to SE in its ability to delineate rat brain C6 glioma in the thalamus region using venous injection of Gd-DTPA.

Acknowledgments

References

1. Nöbauer-Huhmann IM, Ba-Ssalamah A, Mlynarik V, Barth M, Schoggl A, Heimberger K, et al. Magnetic resonance imaging contrast enhancement of brain tumors at 3 tesla versus 1.5 tesla. Invest Radiol 2002;37:114–9.
2. Trattnig S, Ba-Ssalamah A, Noebauer-Huhmann IM, Barth M, Wolfsberger S, Pinker K, et al. MR contrast agent at high-field MRI (3 Tesla). Top Magn Reson Imaging 2003;14:365–75.
3. Ba-Ssalamah A, Nöbauer-Huhmann IM, Pinker K, Schibany N, Prokesch R, Mehrain S, et al. Effect of contrast dose and field strength in the magnetic resonance detection of brain metastases. Invest Radiol 2003;38:415–22.
4. Biswas J, Nelson CB, Runge VM, Wintersperger BJ, Baumann SS, Jackson CB, et al. Brain tumor enhance-ment in magnetic resonance imaging: comparison of signal-to-noise ratio (SNR) and contrast-to-noise ratio (CNR) at 1.5 versus 3 tesla. Invest Radiol 2005;40: 792–7.
5. Runge VM, Biswas J, Wintersperger BJ, Baumann SS, Jackson CB, Herborn CU, et al. The efficacy of gadobenate dimeglumine (Gd-BOPTA) at 3 Tesla in brain magnetic resonance imaging: comparison to 1.5

Tesla and a standard gadolinium chelate using a rat brain tumor model. Invest Radiol 2006;41:244–8.

6. Chappell PM, Pelc NJ, Foo TK, Glover GH, Haros SP, Enzmann DR. Comparison of lesion enhancement on spin-echo and gradient-echo images. Am J Neuroradiol 1994;15:37–44.

7. Rand S, Maravilla KR, Schmiedl U. Lesion enhancement in radio-frequency spoiled gradient-echo imaging: theory, experimental evaluation, and clinical implications. Am J Neuroradiol 1994;15:27–35.

8. Pui MH, Fok EC. MR imaging of the brain: comparison of gradient-echo and spin-echo pulse sequences. Am J Roentgenol 1995;165:959–62.

9. Fellner F, Holl K, Held P, Fellner C, Schmitt R, Bohm-Jurkovic H. A T1-weighted rapid three-dimensional gradient-echo technique (MP-RAGE) in preoperative MRI of intracranial tumours. Neuroradiology 1996;38: 199–206.

10. Li D, Haacke EM, Tarr RW, Venkatesan R, Lin W, Wielopolski P. Magnetic resonance imaging of the brain with gadopentetate dimeglumine-DTPA: comparison of T1-weighted spin-echo and 3D gradient-echo sequences. J Magn Reson Imaging 1996;6:415–24.

11. Elster AD. How much contrast is enough? Dependence of enhancement on field strength and MR pulse sequence. Eur Radiol 1997;7 Suppl 5:276–80.

12. Fischbach F, Bruhn H, Pech M, Neumann F, Ricke J, Felix R, et al. Efficacy of contrast medium use for neuroimaging at 3.0 T: utility of IR-FSE compared to other T1-weighted pulse sequences. J Comput Assist Tomogr 2005;29:499–505.

13. Raila FA, Bowles AP Jr, Perkins E, Terrell A. Sequential imaging and volumetric analysis of an intracerebral C6 glioma by means of a clinical MRI system. J Neurooncol 1999;43:11–7.

14. Thorsen F, Ersland L, Nordli H, Enger PO, Huszthy PC, Lundervold A, et al. Imaging of experimental rat gliomas using a clinical MR scanner. J Neurooncol 2003;63:225–31.

15. Blanchard J, Mathieu D, Patenaude Y, Fortin D. MR-pathological comparison in F98-Fischer glioma model using a human gantry. Can J Neurol Sci 2006;33: 86–91.

16. Wansapura JP, Holland SK, Dunn RS, Ball WS Jr. NMR relaxation times in the human brain at 3.0 tesla. J Magn Reson Imaging 1999;9:531–8.

NOTE

Acceleration of Monte Carlo-based scatter compensation for cardiac SPECT

A Sohlberg[1,2], H Watabe[1] and H Iida[1]

[1] National Cardiovascular Center Research Institute, 5-7-1 Fujishiro-dai, Suita City, 565-8565 Osaka, Japan
[2] HERMES Medical Solutions, Skeppsbron 44, 111 30 Stockholm, Sweden

E-mail: antti.sohlberg@hermesmedical.com

Abstract

Single proton emission computed tomography (SPECT) images are degraded by photon scatter making scatter compensation essential for accurate reconstruction. Reconstruction-based scatter compensation with Monte Carlo (MC) modelling of scatter shows promise for accurate scatter correction, but it is normally hampered by long computation times. The aim of this work was to accelerate the MC-based scatter compensation using coarse grid and intermittent scatter modelling. The acceleration methods were compared to un-accelerated implementation using MC-simulated projection data of the mathematical cardiac torso (MCAT) phantom modelling ^{99m}Tc uptake and clinical myocardial perfusion studies. The results showed that when combined the acceleration methods reduced the reconstruction time for 10 ordered subset expectation maximization (OS-EM) iterations from 56 to 11 min without a significant reduction in image quality indicating that the coarse grid and intermittent scatter modelling are suitable for MC-based scatter compensation in cardiac SPECT.

1. Introduction

The quality of single proton emission computed tomography (SPECT) is degraded by attenuation, collimator blurring and scatter. Whereas attenuation and collimator blurring can nowadays be corrected in clinically acceptable times, accurate and efficient scatter correction has been proven to be a more difficult problem. This is mainly due to the fact that the shape of the scatter point-spread function depends on the location inside the object and can be very difficult to parametrize.

One very promising recently presented scatter compensation method is the Monte Carlo (MC)-based scatter correction by Beekman *et al* (2002). In this method, a MC simulator is used as a forward-projector for scatter in the ordered subset expectation maximization

N277

(OS-EM) algorithm (Hudson and Larkin 1994). MC-based scatter modelling is expected to be especially advantageous in areas where the attenuating media is highly non-uniform such as the thorax, because it can faithfully produce the complex shape of the scatter response function. The MC-based scatter compensation has been shown to outperform the common triple-energy window scatter compensation method in terms of contrast and myocardial lesion detectability (Xiao *et al* 2006). Unfortunately, despite the considerable advances made in MC-based scatter compensation its widespread utilization in clinical practice can still be limited by long computation times.

Kadrmas *et al* (1998) have presented two simple and effective acceleration methods for reconstruction-based scatter compensation. The first of these approaches is the coarse grid scatter modelling method, which calculates the scatter contribution using sparser grid than is used in the actual reconstruction. The second approach is the intermittent scatter modelling method, where scatter is modelled only during the first couple of OS-EM iterations and then held as a constant additive factor for the later iterations. Both of these approaches are based on the assumption that the scatter response contains mainly low-frequency components and can thus be modelled with a relatively large voxel size and not during the last OS-EM iterations. Kadrmas *et al* presented their acceleration methods for the effective scatter source estimation method (Frey and Tsui 1996) and showed that the performance of the accelerated scatter compensation was very similar to the performance of the standard (un-accelerated) scatter correction.

The goal of this work was to implement the coarse grid and intermittent scatter modelling methods for MC-based scatter compensation and to evaluate their performance in case of ^{99m}Tc cardiac SPECT.

2. Materials and methods

2.1. Implementation of the MC simulator

MC simulations are based on sampling radioactive decays within a source volume and following their interactions inside the attenuating media. Our MC simulator uses four different maps in the simulations: emission map for setting photons to be tracked, density map for sampling interactions and primary and scatter maps for storing photon weights. The history of each photon (primary or scatter) in our simple MC simulator is tracked shortly as follows:

(1) If the simulated photon is a primary the primary map is updated. Otherwise direction cosines are sampled and random walk is started for the scatter photon.

(2) Photon interaction points are calculated using the delta scattering algorithm (Woodcock *et al* 1965), which does not require ray tracing through the attenuating media. The basic principle of delta scattering is that the path-length P between two 'fictious' interaction points is sampled as $P = -\ln(R)/\mu_{max}$, where R is a uniform random number and μ_{max} is the largest attenuation coefficient in the attenuating media (Ljungberg *et al* 2005). At the end of the sampled path a possible interaction is sampled according to established methods or tracking is continued by sampling a new distance P according to the above-mentioned equation.

(3) At each real interaction point photon weight is multiplied by the probability that no photoelectric effect occurred and a copy of the original photon is forced to Compton scatter towards the detector and scatter map is updated according to the convolution-based forced detection approach (de Jong *et al* 2001).

(4) If predetermined number of scattering events has not been reached, the history of the original photon is continued by Compton scatter. New direction cosines are sampled from the Klein–Nishina function and tracking is continued from (2).

After all the photons have been simulated the primary and scatter maps are multiplied by probability that photon emitted from a certain voxel reaches the detector without interaction. Then these maps are convolved with depth-dependent detector response function, which is assumed to be Gaussian. The blurred primary and scatter maps are finally forward-projected to primary and scatter projections.

2.2. Implementation of the reconstruction algorithm with MC-based scatter compensation

The developed MC simulator was included into an OS-EM reconstruction algorithm as forward-projector for the scattered counts as originally proposed by Beekman *et al* (2002). The OS-EM is given by

$$f_j^{new} = \frac{f_j^{old}}{\sum_{i \in S_n} a_{ij}} \sum_{i \in S_n} a_{ij} \frac{p_i}{\sum_k a_{ik} f_k^{old} + s_i}, \tag{1}$$

where f is the reconstructed image, p is the measured projections, j (or k) is the reconstruction voxel index, i is the projection pixel index, a_{ij} is the probability that emission from voxel j is detected in pixel i, s is the MC-based scatter projections and S_n is the nth subset. The image update in OS-EM consists of sequential forward- and back-projection operations. The estimated projections are obtained by forward-projecting the current image estimate $\left(\sum_k a_{ik} f_k^{old}\right)$, and correction terms that are used to update the old image are formed by back-projecting the ratio of the measured and estimated + scatter projections $\left(\sum_{i \in S_n} a_{ij} \frac{p_i}{\sum_k a_{ik} f_k^{old} + s_i}\right)$.

In this work the forward- and back-projectors were implemented as rotation based (Di Bella *et al* 1996). The back-projector included attenuation and detector response compensation and the forward-projector attenuation, detector response and MC-based scatter compensation. Attenuation correction factors for each voxel were calculated simply by summing the rotated attenuation map along columns. Detector response, on the other hand, was modelled by convolving each plane of the reconstruction matrix parallel to the projection plane with collimator response kernel, which was assumed to be Gaussian. The scatter projection for each projection angle was obtained by MC-based forward-projection of the current image estimate.

2.3. Acceleration of MC-based scatter compensation

The coarse grid scatter modelling method was implemented by simply down-sampling the current image estimate (and the attenuation map) into a sparser matrix before the MC-based forward-projection and linearly interpolating the scatter projections back to the original size after forward-projection was finished. In the intermittent acceleration approach the MC-based scatter modelling is performed only in the few early OS-EM iterations and after that the scatter projections are kept fixed for remaining iterations.

2.4. Performance tests

Performance tests were performed using a female version of the mathematical cardiac torso (MCAT) phantom (Tsui *et al* 1994), and the camera parameters are shown in table 1. The MCAT phantom modelled normal human tissue densities in the thorax region and the source distribution presented the ^{99m}Tc uptake with the following relative activities per
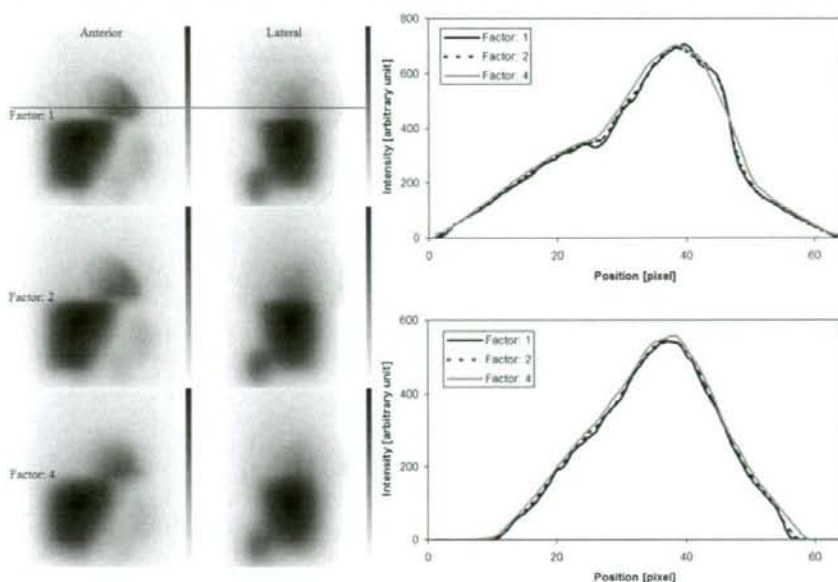
Figure 1. Comparison of scatter projections and profiles obtained with different down-sampling factors (factor: 1 is scatter projection without down-sampling). Upper profile is obtained from the anterior projection and lower from the lateral projection. Locations of the profiles are shown as horizontal lines.

Table 1. Camera parameters for Monte Carlo simulations.

Low-energy high-resolution collimator (4.0 cm hole length, 0.178 cm hole diameter)
0.4 cm intrinsic detector resolution
9.0% energy resolution
15.0% energy window centred on 140 keV
23.0 cm radius of rotation

voxel: myocardium 100, liver 50, kidney 100, spleen 80, lung 5 and rest of the body 2.5. Two lesions (anterior and inferior) with the relative uptake of 2.5 were included in the left myocardium.

The effects of different down-sampling factors in the coarse grid scatter modelling scheme were studied by performing MC simulations using the MCAT phantom. The pixel size was set to 0.625 cm (64 × 64 projection and 64 × 64 image matrix size). Down-sampling factors of 2 (64 × 64 × 64 image matrix down-sampled to 32 × 32 × 32 matrix) and 4 (64 × 64 × 64 image matrix down-sampled to 16 × 16 × 16 matrix size) were investigated. Figure 1 presents anterior and lateral scatter projection images of the MCAT phantom. According to this figure factor 4 produces slightly distorted scatter projections, and thus the down-sampling factor was set to 2 for all the reconstructions accelerated with the coarse grid scatter modelling.

The effect of the number of scatter update iterations was studied by using MCAT projection data simulated using the SIMIND MC simulator (Ljungberg and Strand 1989). The camera parameters for this simulation are again shown in table 1. The number of simulated noise-free
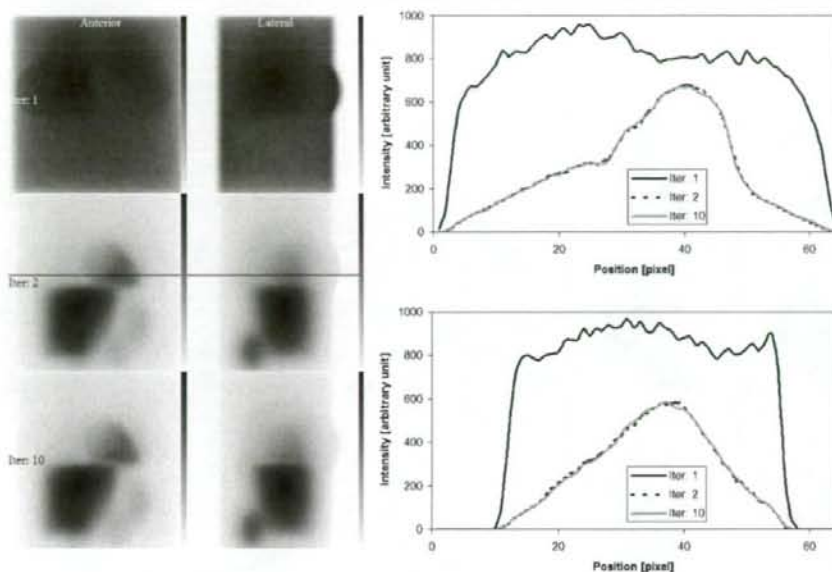
Figure 2. Comparison of different number of scatter update iterations. Upper profile is obtained from the anterior projection and lower from the lateral projection. Locations of the profiles are shown as horizontal lines.

projections was 64 on a 360° orbit and pixel size was 0.3125 cm (128 × 128 projection and 128 × 128 × 128 image matrix size). The projections were collapsed to a 64 × 64 matrix size before the reconstruction. Reconstruction using the noise-free projection data was performed with 16 subsets and 1–10 iterations, and the MC forward-projected scatter projections were saved after every iteration. Figure 2 presents scatter projection images and profiles for different iteration numbers, and these images show that the scatter projections do not change markedly after two iterations. Therefore, in the following performance tests only two scatter iterations were used when intermittent scatter modelling was applied.

The acceleration methods were tested using the same MCAT projection data that were used to find the scatter iterations stopping point. Poisson noise was added to the noise-free projections by setting number of total counts to 5 million. The projections were reconstructed without scatter compensation, with the MC-based scatter compensation but without acceleration, with coarse grid scatter modelling (down-sampling factor of 2), with intermittent scatter modelling (scatter updated during the first two iterations) and with both accelerations applied at the same time. Number of MC simulated photons per projection angle was set to 1.0 million and 16 subsets with 10 iterations were used. After reconstruction images were filtered with a 3D Butterworth filter (order: 5, cutoff: 1.0 cm^{-1}), transverse slices were zoomed and reoriented into short-axis slices. Regions of interest (ROI) were drawn on the normal myocardium, ventricle and on the anterior/inferior defect areas. Normal myocardium to ventricle and normal myocardium to lesion contrasts were calculated.

In addition to Monte Carlo simulations the acceleration methods were also tested using a clinical ^{99m}Tc myocardial stress/rest perfusion study acquired with the Siemens Symbia SPECT/CT scanner. Low-energy high-resolution parallel hole collimators were used, and
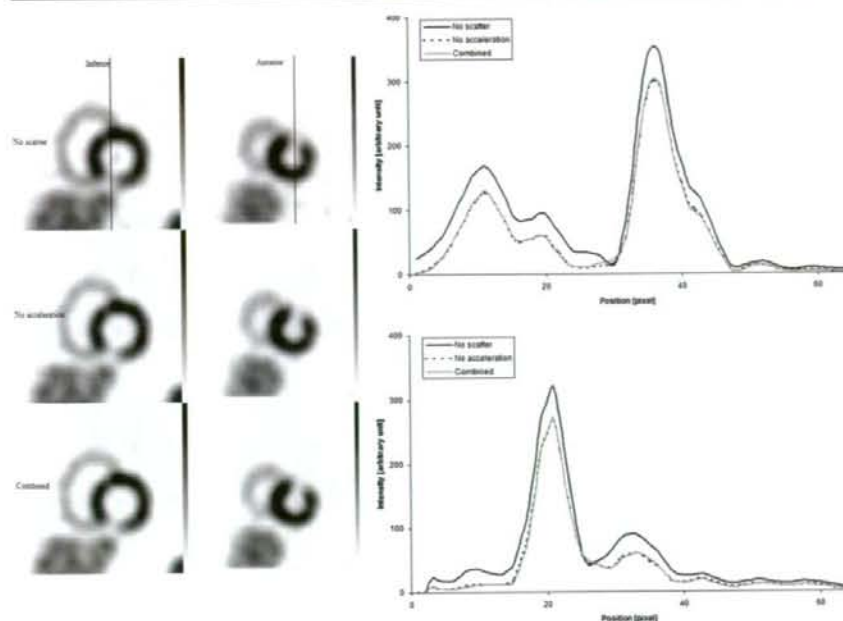
Figure 3. Short-axis slices and profiles through the heart of the MCAT phantom for reconstruction without scatter compensation (no scatter) and with MC-based scatter compensation without acceleration (no acceleration) and with coarse grid + intermittent scatter modelling (combined). Results for other acceleration methods are not shown, because they overlap the coarse grid + intermittent scatter compensation profiles. Upper profile is obtained from the image with inferior lesion and lower with anterior lesion. Locations of the profiles are shown as vertical lines.

Table 2. Lesion-to-normal myocardium and ventricle-to-normal myocardium contrasts for different MC-based scatter compensation acceleration schemes.

Scatter compensation method	Acceleration method	Contrast		
		Anterior	Inferior	Ventricle
No compensation		0.57	0.51	0.80
MC-based	No acceleration	0.64	0.58	0.91
	Coarse grid	0.65	0.59	0.93
	Intermittent	0.62	0.60	0.93
	Coarse grid+intermittent	0.64	0.59	0.93

60 projection angles over a 180° arc were acquired using a symmetric 15% energy window centred at 140 keV.

3. Results

Figure 3 shows short-axis slices and profiles through the left ventricle of the MCAT phantom for reconstruction without scatter compensation and with the MC-based scatter compensation without acceleration and with coarse grid + intermittent scatter modelling. Profiles for the
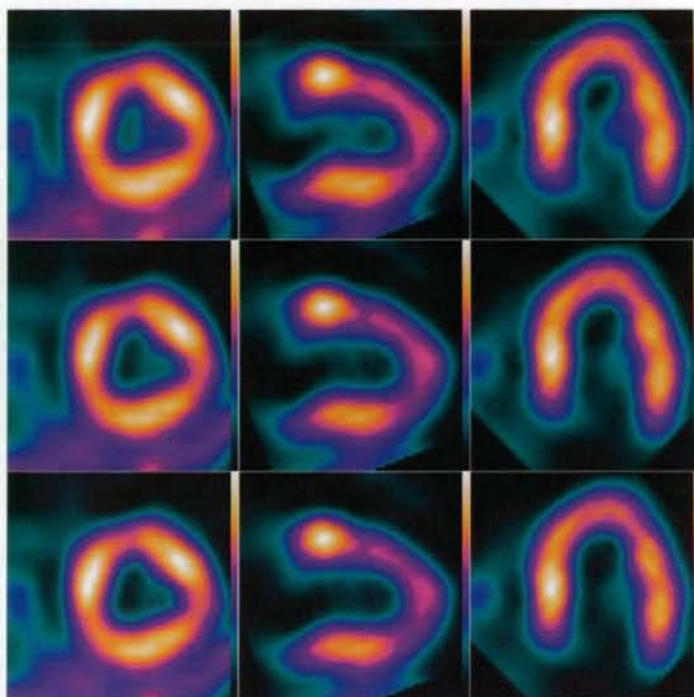
Figure 4. Example short-axis (first column), vertical long-axis (second column) and horizontal long-axis (third column) slices from a clinical rest myocardial perfusion study for reconstruction without scatter compensation (first row), with MC-based scatter compensation without acceleration (second row) and with coarse grid +intermittent scatter modelling (third row).

un-accelerated and accelerated scatter compensation practically overlap indicating similar performance. This same conclusion can also be drawn from table 2, which presents the lesion and ventricle contrasts. All the scatter compensation methods offer very similar contrast values and clearly improve contrast when compared to reconstruction without scatter compensation.

Figure 4 presents results for the resting clinical study (for the stress study the findings in image quality were identical to the resting study). It can be seen that the images reconstructed with and without MC-based scatter compensation acceleration are nearly identical. Table 3 presents the approximate reconstruction times for different scatter compensation methods.

4. Discussion

The aim of this study was to accelerate the MC-based scatter compensation using the coarse grid and intermittent scatter modelling methods. Both of these acceleration methods proved to provide clear improvement in execution times without any marked degradation in image quality when compared to un-accelerated version of MC-based scatter-compensation (tables 2 and 3, figures 3 and 4). The greatest improvement in terms of speed was obtained by combining the two acceleration methods.

Table 3. Approximate reconstruction times (10 iterations, 16 subsets and 1 million photons per projection) for different MC-based scatter compensation acceleration schemes. Reconstructions were performed using 2.33 GHz Pentium processor with 8 GB RAM.

Scatter compensation method	Acceleration method	Time (min)
No compensation		0.8
MC-based	No acceleration	55.6
	Coarse grid	53.4
	Intermittent	11.6
	Coarse grid + intermittent	11.2

The comparison studies for the scatter compensation methods were performed with $64 \times 64 \times 64$ matrix sizes and coarse-grid down-sampling factor of 2 was used, because larger down-sampling factors could not fully preserve the details of the scatter projections (figure 1). With larger matrix sizes than $64 \times 64 \times 64$ larger down-sampling factors could probably be used for higher acceleration. This was not studied in this work, because in the case of cardiac SPECT $64 \times 64 \times 64$ matrix size is usually considered the standard.

The acceleration achieved with the coarse grid scatter modelling depends also on the implementation of the MC simulator that is used in the forward-projection. As mentioned, our MC simulator is based on the delta scattering technique (Woodcock *et al* 1965), which allows calculation of the photon interaction points without time-consuming ray tracing. Therefore, the coarse-grid scatter modelling provided acceleration mainly because the collimator response and attenuation modelling were performed with the sparser matrix. In the case of 1 million simulated photons per projection the time needed to model the collimator response and attenuation is, however, only a small fraction of the time that is spent in sampling the various probability distributions in the MC calculations. Thus the speed-up provided by the coarse-grid scatter modelling is quite small, but can be much greater if a smaller number of simulated photons are used. In addition, if a ray-tracing-based MC algorithm is used instead of delta scattering, coarse-grid scatter modelling will probably increase the speed much more, because the efficiency of ray tracing depends heavily on the matrix size.

In this study the scatter projections were not noticed to change markedly after two iterations, and thus in the intermittent scatter modelling scheme scatter projections were updated only during the first two OS-EM iterations. The number of scatter iterations needed may, however, depend on the imaging situation as mentioned by Kadrmas *et al* (1998) and should therefore be checked before using intermittent scatter modelling as an acceleration method.

One important thing that was not considered in detail in this work is the number of simulated photons per projection. We chose the 1 million photons per projection according to our preliminary studies, where we compared the quality of images reconstructed using different number of simulated photons and noticed that using over 1 million photons per projection does not lead to a significant increase in image quality. The performance of MC-based scatter compensation is, however, quite complicated because it is not only influenced by the number of simulated photons but also by the interplay of noise in attenuation map/projection data and the number of simulated photons. Therefore, a detailed study of noise effects, e.g. similar to the one presented by de Wit *et al* (2005), is probably needed in the future. If different number of photons per projection are to be used the speed-up factors might not be the same as in table 2.

Faster reconstruction times with MC-based scatter compensation than those shown in table 3 have been presented in the literature (e.g. de Wit *et al* (2005) and Xiao *et al* (2006)). This

speed difference is probably mainly related to algorithm implementation. Our reconstruction algorithm is not yet fully optimized, and we believe that we can greatly reduce the execution time of our reconstruction. In addition to direct code optimization, we are also planning to parallelize our code for multi-core processors. The acceleration methods presented in this work should be very suitable for different parallelization schemes, because they do not affect the general structure of the OS-EM reconstruction algorithm.

5. Conclusions

We conclude that both the coarse grid and the intermittent scatter modelling methods are suitable for accelerating MC-based scatter compensation, and with these methods MC-based scatter compensation is a promising alternative for clinical cardiac SPECT.

Acknowledgment

References

Beekman F J, de Jong H W A M and van Geloven S 2002 Efficient fully 3-D iterative SPECT reconstruction with Monte Carlo-based scatter compensation *IEEE Trans. Med. Imaging* **21** 867–77

de Jong H W A M, Slijpen E T P and Beekman F J 2001 Acceleration of Monte Carlo SPECT simulation using convolution-based forced detection *IEEE Trans. Nucl. Sci.* **48** 58–64

de Wit T C, Xiao J and Beekman F J 2005 Monte Carlo-based statistical SPECT reconstruction: influence of number of photon tracks *IEEE Trans. Nucl. Sci.* **52** 1365–9

Di Bella E V R, Barclay A B, Eisner R L and Schafer R W 1996 A comparison of rotation-based methods for iterative reconstruction algorithms *IEEE Trans. Nucl. Sci.* **43** 3370–6

Frey E C and Tsui B M W 1996 A new method for modelling the spatially-variant, object dependent scatter response function in SPECT *IEEE Nuclear Science Symp.and Medical Imaging Conf. Record* pp 1082–6

Hudson H M and Larkin R S 1994 Accelerated image reconstruction using ordered subsets of projection data *IEEE Trans. Med. Imaging* **13** 601–9

Kadrmas D J, Frey E C, Karimi S S and Tsui B M W 1998 Fast implementations of reconstruction-based scatter compensation in fully 3D SPECT image reconstruction *Phys. Med. Biol.* **43** 857–73

Ljungberg M, Larsson A and Johansson L 2005 A New collimator simulation in SIMIND based on the Delta-Scattering technique *IEEE Trans. Nucl. Sci.* **52** 1370–5

Ljungberg M and Strand S-E 1989 A Monte Carlo program for the simulation of scintillation camera characteristics *Comput. Methods Programs Biomed.* **29** 257–72

Tsui B M W, Zhao X D, Gregoriou G K, Lalush D S, Frey E C, Johnston R E and McCartney W H 1994 Quantitative cardiac SPECT reconstruction with reduced image degradation due to patient anatomy *IEEE Trans. Nucl. Sci.* **41** 2838–44

Woodcock E, Murphy T, Hemmings P and Longworth S 1965 Techniques used in the GEM code for Monte Carlo neutronics calculations in reactors and other systems with complex geometry *Proc. Conf. for Applications of Computing Methods to Reactor Problems* p 557

Xiao J, de Wit T C, Staelens S G and Beekman F J 2006 Evaluation of 3D Monte Carlo-based scatter correction for ^{99m}Tc cardiac perfusion SPECT *J. Nucl. Med.* **47** 1662–9

Use of a Clinical MRI Scanner for Pre-clinical Research on Rats

Akihide YAMAMOTO [1,2], Hiroshi SATO[3], Jun-ichiro ENMI[1],Kenji ISHIDA[1],

Takayuki OSE[1], Atsuomi KIMURA[2], Hideaki FUJIWARA[2], Hiroshi WATABE[1,2],

Takuya HAYASHI[1,2], Hidehiro IIDA[1,2] *

1.   Department of Investigative Radiology, Advanced Medical-Engineering

Center, National Cardiovascular Center-Research Institute, 5-7-1, Fujishiro-dai,

Suita, Osaka, 565-8565, Japan.

2.   Department of Medical Physics and Engineering, Division of Health

Sciences, Graduate School of Medicine, Osaka University, 1-7, Yamada-oka, Suita,

Osaka, 565-0871, Japan.

3.   Laboratory for Diagnostic Solution, Advanced Medical-Engineering Center,

National Cardiovascular Center-Research Institute, 5-7-1, Fujishiro-dai, Suita,

Osaka, 565-8565, Japan.

*Corresponding author: Hidehiro Iida, D.Sc., Ph.D.

Department of Investigative Radiology, Advanced Medical-Engineering Center,

National Cardiovascular Center-Research Institute

*5-7-1, Fujishiro-dai, Suita, Osaka, 565-8565, Japan

Phone: +81-6-6833-5012 ex 2559, Fax: +81-6-6835-5429, iida@ri.ncvc.go.jp

RUNNING HEAD: Use of a 3-Tesla MRI Scanner for rat brain imaging

Abstract (150words)

This study focused on evaluating the feasibility of rat brain imaging by use of a human whole-body 3-Tesla magnetic-resonance-imaging (MRI) scanner with developed transmit-and-receive radiofrequency coils.

The T_1-, T_2- weighted images obtained showed reasonable contrast. Acquired contrast-free time-of-flight magnetic-resonance-angiography images clearly showed the cortical middle-cerebral-artery (MCA) branches, and inter-hemispheric differences could be observed.

Dynamic-susceptibility-contrast MRI at a 1.17 mm^3 voxel resolution, performed three times following administration of gadolinium-diethylenetriamine pentaacetic acid (Gd-DTPA, 0.1 mmol/kg), demonstrated that the arterial input function (AIF) can be obtained from the MCA region, yielding cerebral blood flow (CBF), cerebral blood volume, and mean transit time (MTT) maps. The parietal-cortex (Pt)-to-hypothalamus (HT) CBF ratio was 45.11±2.85 %, and the MTT was 1.29±0.40 sec in the Pt and 2.32±0.17 sec in the HT region. A single dose of Gd-DTPA enabled assessment of AIF within the MCA territory and of quantitative CBF in rats.

2

Introduction

Magnetic-resonance-imaging (MRI) has been widely used in pre-clinical research on experimental small animals. Studies have typically been aimed at understanding the pathophysiologic status and for evaluating the efficacy/side effects of newly developed treatments, such as pharmaceutical and regenerative medicine. Recently, a different idea has surfaced: the use of a human whole-body MRI scanner for small-animal imaging [1]. Although small-animal dedicated scanners are superior to clinical scanners in terms of providing a better signal-to-noise ratio, the available pulse sequences are different from those on clinical scanners, and the magnetic field strength is often much higher. Small-animal imaging with clinical scanners is important for directly addressing clinical questions and/or identifying the source of signal changes, including various disease conditions in a clinical setting.

Smith et al. [2] demonstrated that anatomic brain T_1- weighted (T_1W) images and T_2-weighted (T_2W) images can be obtained for healthy rats by use of a 1-Tesla clinical MRI scanner with a specially designed radiofrequency (RF) coil, given a reasonable spatial resolution ($0.1953 \times 0.1953 \times 2.5$ mm, 24 min of T_1W and 48 min of T_2W). The image contrast was sufficiently high for distinguishing the cortical gray matter from the white matter (corpus callosum (CC)), as well as the lateral ventricle (LV) and interpeduncular cistern (IPC) from the thalamus (Thal). Guzman et al. [3] employed a clinical 1.5-Tesla MRI scanner with a commercially available RF coil and demonstrated that both T_1W and T_2W images can be obtained with good contrast, a

3

reasonable spatial resolution of $0.3125 \times 0.3125 \times 1.5$ mm, and an acquisition time of 19 min 51 sec, as well as $0.35156 \times 0.375 \times 1.5$ mm at 8 min 34 sec, corresponding to T_1W and T_2W images, respectively. Other investigators [4] applied a clinical 1.5-Tesla MRI scanner with a 3-inch-diameter circular receive-only surface coil to assess anatomic images. Their images can be of use in the evaluation of the pathophysiologic status of stroke [4] and cancer [5, 6], as well as the effects of neural excitotoxicity [3]. There were also several studies with a clinical 3-Tesla MRI scanner fitted with commercial and/or hand-made RF coils for investigating the pathophysiology of stroke [7, 8] and brain tumors in rats [6, 9, 10]. Generally speaking, anatomic images with better contrast can be obtained in a stronger magnetic field, although there are additional factors which may influence the signal-to-noise ratio (SNR) or spatial resolution of anatomic images. Contrast-free time-of-flight magnetic-resonance angiography (TOF-MRA) can also be obtained on rats with a reasonable spatial resolution by use of a clinical 3-Tesla MRI scanner with a single-turn solenoid coil [11].

Dynamic-susceptibility-contrast MRI (DSC-MRI) [12] has been widely used in clinical diagnosis, particularly in patients with stroke [13-19] and tumors [20]. The application of clinical MRI scanners has been extended to DSC-MRI studies of small-animals with stroke [21, 22] and tumors [23] by use of a 1.5-Tesla MRI scanner. Up to now, small-animal studies have been performed on 1.5-Tesla MRI scanners only, and 3-Tesla scanners have not yet been employed. This is largely attributed to

4

the fact that the susceptibility-induced inhomogeneous magnetic field may cause more serious distortion of the images at a higher static magnetic field. In DSC-MRI studies, the echo planar imaging (EPI) technique is mainly used because fast acquisition is required for accurate tracking of the bolus passage of MR contrast agents. The EPI technique, however, is very sensitive to magnetic field inhomogeneity, and thus the EPI images of small-animal brains may be severely distorted. The gradient slew rate (SR) is not high enough to support sufficiently short echo spacing period, when clinical scanners are used for high-spatial resolution imaging of small objects. Moreover, injected materials may cause further distortion [24]. Currently, it is unknown how severely dynamic EPI images of small-animal brains will become distorted on a 3-Tesla clinical scanner. The arterial input function (AIF) is also questionable. To the best of our knowledge, no DSC-MRI studies of small-animal brains on 3-Tesla clinical scanners have been reported.

This study was aimed at evaluating the feasibility of a human whole-body 3-Tesla MRI system developed for small animals, particularly for DSC-MRI with a single dose of gadolinium-diethylenetriamine pentaacetic acid (Gd-DTPA). The quality of various images, including the anatomic T_1W images, T_2W images, TOF-MRA images, and DSC images, was tested, and the availability of the AIF obtained from the rat brain was evaluated.

Materials and Methods

Subjects

5

105

The subjects were three healthy adult rats supplied by Japan SLC, Inc. (Shizuoka, Japan). All three rats were males, and they ranged in age from 20 to 24 weeks. Their weight range was between 400 to 600 grams. Anesthesia was administered with an intramuscular injection of ketamine (33 mg/kg; Daiichi-Sankyo Co., Ltd., Tokyo, Japan) and xylazine (6.6 mg/kg; Bayer Yakuhin, Ltd., Osaka, Japan). The first rat (Sprague-Dawley, SD) was used for T_1-W and T_2W imaging of the whole brain. The second rat, also a SD, was used for contrast-free TOF-MRA imaging. The third was a Wistar rat, which was used for a Gd-DTPA (0.1 mmol/kg; Bayer Yakuhin, Ltd., Osaka, Japan)-enhanced DSC-MRI sequence. Experiments were carried out according to the protocol approved by the Local Committee for Laboratory Animal Welfare, National Cardiovascular Center, Osaka, Japan.

MRI acquisition

A human whole-body 3-Tesla MRI scanner (Signa, GE Healthcare, Milwaukee, WI, USA) equipped with a 55-cm bore was employed in this study. The gradient coil system was capable of providing the maximum amplitude of the gradient at 40 mT/m, and at an SR of 150 T/m/s. All sequence programs employed in this study were designed for clinical studies.

Two solenoid coils designed for rats were specially developed to cover the whole brain, which are capable of both transmitting and receiving RF pulses. The three-turn solenoid coil, which had a diameter of 42 mm and a length along a cylindrical axis of 18 mm, was attached to an apparatus made of acrylic mold as

6